

# In situ index-of-refraction measurements of the South Polar firn with the RICE detector

Ilya KRAVCHENKO,<sup>1</sup> David BESSON,<sup>2</sup> Josh MEYERS<sup>2</sup>

<sup>1</sup>Laboratory for Nuclear Science, Massachusetts Institute of Technology, Cambridge, Massachusetts 02139, USA

<sup>2</sup>Department of Physics and Astronomy, University of Kansas, Lawrence, Kansas 66045-2151, USA

E-mail: dzb@mail.lns.cornell.edu

**ABSTRACT.** Using the RICE (Radio Ice Cherenkov Experiment) detector at the South Pole, we have estimated the variation in the index of refraction ( $n$ ) of the firn, as a function of elevation ( $z$ ) measured from the surface down to  $z = -150$  m. Measurements were made by lowering a dipole transmitter into a dry (5 in (127 mm) caliber) borehole, originally drilled for the RICE experiment in 1998, and determining signal arrival times, as a function of transmitter depth, in the englacial RICE receiver array. We clearly confirm the expected correlation of  $n(z)$  with ice density. Our measurements are in fair agreement with previous laboratory characterizations of the dielectric properties of ice cores. These are the first such in situ measurements to be performed at the South Pole.

## INTRODUCTION

The Antarctic ice sheet has provided an extraordinary laboratory for a variety of scientific purposes, including measurements of the Earth's climatological history (Paterson, 1994), and studies of the early solar system using meteorites collected on the Antarctic surface (Dodd, 1989). The AMANDA (Antarctic Muon And Neutrino Detector Array; Ahrens and others, 2003a,b,c), ICECUBE (Karle, 2002), RICE (Radio Ice Cherenkov Experiment; Kravchenko and others, 2003a,b) and ANITA (ANTarctic Impulsive Transient Apparatus) collaborations seek to use the solid, large-volume and extraordinarily transparent (for wavelengths  $>100$  nm) ice sheet as a neutrino target. The pioneering AMANDA experiment has successfully demonstrated the viability of englacial neutrino detection through the reconstruction of thousands of atmospheric muon neutrinos (Niessen, 2003) using a photomultiplier tube (PMT) array. ICECUBE plans to extend the coverage and acceptance of AMANDA through a larger-scale ( $\sim 1$  km<sup>2</sup> effective area) PMT deployment, sensitive to Cherenkov radiation in the near-ultraviolet (250–400 nm) region of the electromagnetic spectrum.

The RICE and ANITA experiments also seek to detect neutrinos interacting in the Antarctic ice sheet. Whereas AMANDA's sensitivity is maximal for muon neutrinos, the RICE and ANITA experiments focus on electron neutrino detection. This is done by measuring the Cherenkov radiation produced by neutrino interactions in polar ice, albeit at lower frequencies (100 MHz–1 GHz) than AMANDA/ICECUBE. The RICE experiment consists of an array of 17 in-ice dipole receivers, deployed at depths of  $-100$  to  $-350$  m, and read out into digital oscilloscopes. Calibration techniques and event reconstruction (Kravchenko and others, 2003b), as well as results on the neutrino flux at Earth (Kravchenko and others, 2003a), are presented elsewhere. Although the measurable neutrino flux is primarily due to interactions below the array, radio-frequency (RF) backgrounds due to air showers or above-surface anthropogenic sources require reconstruction of sources viewed through the firn. Similarly, reconstruction of neutrino candidate interactions by the balloon-borne ANITA experiment requires ray tracing through the firn and into the ice itself. In order to have an

accurate estimate of the neutrino energy, it is necessary to know the exact location of the neutrino interaction in the ice. Due to bending of rays through the firn, it is therefore important to have an accurate characterization of the variation of the dielectric constant  $\varepsilon$  with depth in polar ice ( $\text{Re}(\varepsilon) = \varepsilon' = n^2$ ).

The variable index-of-refraction of the firn has another important experimental consequence, due to the fact that any change in the index of refraction across a boundary introduces non-zero reflections at that interface. The corresponding reflection and transmission coefficients, for the perpendicular and parallel components of the incident electric field ( $r_{\perp}$  and  $r_{\parallel}$  and  $t_{\perp}$  and  $t_{\parallel}$ , respectively), are given by the standard 'Fresnel equations for dielectric media', in terms of the angle of incidence ( $\theta_i$ ) and angle of transmission ( $\theta_t$ ),

$$r_{\perp} = \frac{(n_i \cos \theta_i) - (n_t \cos \theta_t)}{(n_i \cos \theta_i) + (n_t \cos \theta_t)} = -\frac{\sin(\theta_i - \theta_t)}{\sin(\theta_i + \theta_t)},$$

$$r_{\parallel} = \frac{(n_t \cos \theta_i) - (n_i \cos \theta_t)}{(n_i \cos \theta_t) + (n_t \cos \theta_i)} = \frac{\tan(\theta_i - \theta_t)}{\tan(\theta_i + \theta_t)},$$

$$t_{\perp} = \frac{2 \sin(\theta_i) \cos(\theta_i)}{\sin(\theta_i + \theta_t)},$$

$$t_{\parallel} = \frac{2 \sin(\theta_i) \cos(\theta_i)}{\sin(\theta_i + \theta_t) \cos(\theta_i - \theta_t)}.$$

Thus, the measured RICE signal strength for above-ice sources, as viewed by below-firn receivers (or vice versa), depends on the degree of variation in the index of refraction. For the case of the balloon-borne ANITA experiment, the dielectric contrast at the surface (i.e. the air-ice interface) determines the critical angle, and therefore also dictates the volume of ice which is visible to the balloon. Measurements of the index-of-refraction at the bottom of the ice sheet, and therefore the strength of the return echo when the ice is probed by ground-penetrating radar (GPR) from the surface, are also used to discriminate between pure ice-rock vs 'dirty' ice-rock vs water-ice interfaces. This also has importance in understanding the features beneath the ice-covered surfaces of Jovian moons such as Europa.

## PREVIOUS RESULTS

The dielectric response of a given medium to an electromagnetic excitation of angular frequency  $\omega$  is often formulated in an atomic-resonator model (Hecht, 2001). In such a model, it is not surprising that the index-of-refraction of water varies substantially between the liquid and solid phases, or as a function of impurity. The dielectric properties of ice have been well studied (Bogorodsky and others, 1985). We present below only a subsample of the measurements that have been made thus far. The bulk of the measurements of polar ice properties have been performed in the laboratory using cored samples of Arctic or Antarctic ice, or on laboratory-prepared samples of ice at a given temperature, impurity level and density. Deviations between in situ vs laboratory dielectric measurements can then give information on the impurity content of in situ samples (Fujita and others, 2000).

## Laboratory measurements

Resonance techniques can be used to make high-precision measurements of ice dielectric response under controlled conditions. Such techniques lend themselves most readily to GHz regime measurements, corresponding to the size scale of typical laboratory samples. In the resonator model, the frequency dependence of  $n$  in the 0.1–1 GHz regime is negligible for cold ice; the temperature dependence has been measured in the laboratory to be very small:  $\epsilon' = 3.1884 + 9.1T^{-4}$ , with  $T$  the temperature in  $^{\circ}\text{C}$  (Gough, 1972; Johari and Charette, 1975; Mätzler and Wegmüller, 1987). Over the profile of a typical Antarctic ice core, this corresponds to an expected variation of  $<1\%$ . A dedicated dielectric profiling device, capable of measuring dielectric properties of ice over a wide frequency range (Moore and Paren, 1987; Wilhems and others, 1998; Wilhems, 2000), has been used to directly measure the complex dielectric constant over the first 100 m of core B32 (Eisen and others, 2003) taken in 1997/98 from Dronning Maud Land, Antarctica, at an elevation of 2900 m (Oerter and others, 2000). Those data, for both  $\text{Re}(\epsilon) (= \epsilon')$  and  $\text{Im}(\epsilon) (= \epsilon'')$ , are reproduced in Figure 1. Shown are the real (refractive) and imaginary (absorptive) components of the dielectric constant over the length of the measured core. At 100 m depth, these measurements correspond to  $n = \sqrt{3.0} = 1.732$ .

## Field measurements

The real part of the dielectric constant is often parameterized simply in terms of the density of polar ice as  $n(z) = 1 + 0.86\rho(z)$ , where  $\rho(z)$  is the density at a given depth  $z$ , taken as positive upwards from the surface. This profile is not universal for all locations in Antarctica, and depends on such variables as accumulation rates, impurity content, temperature profiles and glacial age. At the Pole, for instance, measurements of the temperature at  $z = -10$  m ( $-51^{\circ}\text{C}$ ), as well as the nominal depth of the firm–ice transition ( $-115$  m), are considerably different from those at  $z = -10$  m at Little America ( $-24^{\circ}\text{C}$  and  $-51$  m) or Byrd Station ( $-28^{\circ}\text{C}$  and  $-64$  m) (Paterson, 1994). Assuming that the density at a given depth is directly dependent on the overburden of ice at that depth, one would expect that the density profile is continuous and follows an exponential. An empirical depth–density relation has been given by Schytt (1958) as  $\rho(z) = \rho_{\text{ice}} - (\rho_{\text{ice}} - \rho_{\text{surface}})\exp(-C|z|)$ , where  $\rho_{\text{ice}}$  is the asymptotic density of polar ice ( $917\text{ kg m}^{-3}$ ),

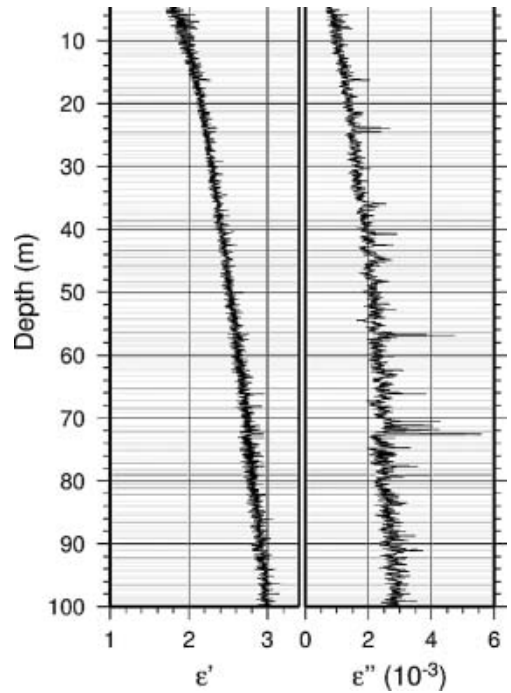


**Fig. 1.** Complex dielectric constant, measured from core B32 in Dronning Maud Land, from Eisen and others (2003). (a) Ordinary relative permittivity  $\epsilon'$ ; (b) dielectric loss factor  $\epsilon''$ , measured at 250 kHz and scaled to 200 MHz, using:  $\epsilon = \epsilon' - i\epsilon'' = \epsilon' - i\sigma(\epsilon_0\omega) - 1$ , where the real part  $\epsilon'$  is the ordinary relative permittivity of the medium, and the imaginary part  $\epsilon''$  is the dielectric loss factor. The latter can be expressed as a function of conductivity  $\sigma$ , angular frequency  $\omega$  and permittivity of vacuum  $\epsilon_0$  (as indicated) and allows scaling of the absorptive portion of the dielectric constant from kHz to MHz frequencies. Gray horizontal bars indicate dielectric-profiling data gaps. (Reprinted from [http://www.agu.org/pubs/sample\\_articles/cr/2002GL016403/2.shtml](http://www.agu.org/pubs/sample_articles/cr/2002GL016403/2.shtml).)

$\rho_{\text{surface}}$  is the density of the snow at the surface (for the South Pole, we use  $359\text{ kg m}^{-3}$  (Costas, 1963), although other measurements in Antarctica give values that vary significantly (e.g. Narita and others, 1978)), and  $C$  is a constant, approximately equal to  $1.9/t_{\text{firm}}$ , where  $t_{\text{firm}}$  is the firm thickness (in m).

Radio-echo soundings have been used extensively to map the bed topography under the polar ice sheets. In cases where the absolute depths of reflecting layers within the ice can be directly measured by use of probes along a pre-existing core (e.g. from the Greenland Icecore Project (GRIP)), a value for the index of refraction, averaged down to the depth of a given reflecting layer, can be determined using measured return times. (In practice, however, it is easiest to use such radio-echo soundings to determine the asymptotic value of the index of refraction below the firm, and use laboratory measurements to infer the index of refraction through the firm.) Such an approach allows precise determinations of the electromagnetic wave speed  $v$  through polar ice at RF frequencies. Hempel and others (2000) obtained  $v = 168.1 \pm 0.5\text{ m } \mu\text{s}^{-1}$  at 35 MHz; this wave speed corresponds to  $n = 1.783 \pm 0.005$  below the firm. This measurement is consistent with the value ( $z < -50$  m) obtained by tracking a target lowered into the ice on Whillans Ice Stream, West Antarctica (Clarke and Bentley, 1994). That experiment determined  $v = 170 \pm 4\text{ m } \mu\text{s}^{-1}$  ( $n = 1.764 \pm 0.004$ ) at 80 MHz in the region below  $z = -50$  m. At shallower depths those data

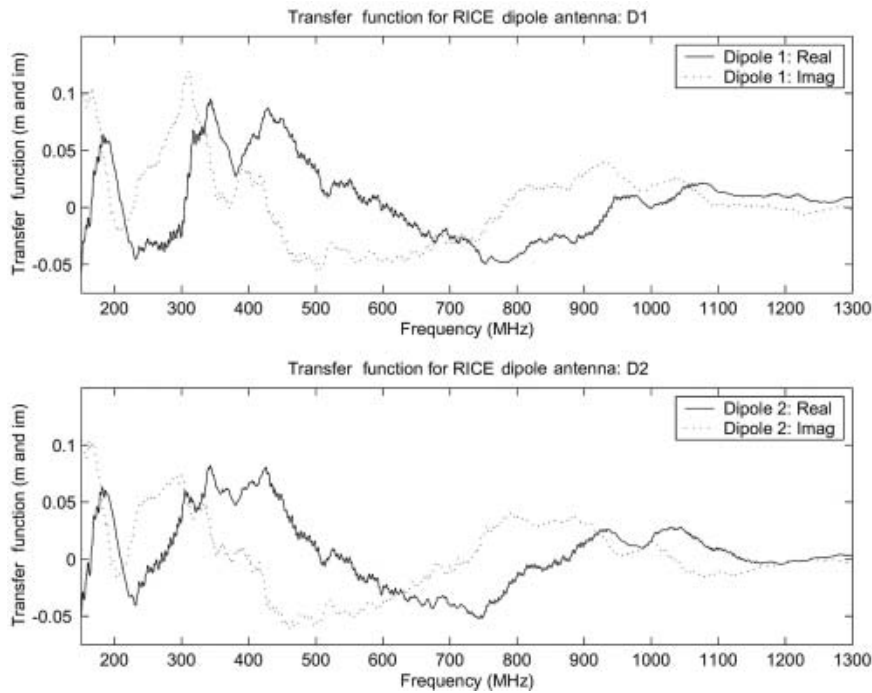


**Fig. 2.** RICE dipole transfer function, measured in air for two typical RICE dipoles.

imply a linear dependence of index-of-refraction on depth and disfavor a higher-order variation, whereas the measured density profile of the firn would suggest a non-linear variation of  $n(z)$ . The authors suggested that the presence of crevasses may be responsible for this apparently linear dependence, whereas there are no such features in the ice at South Pole.

There is a vast body of literature documenting earlier measurements of the the electromagnetic wave speed (averaged through the densest ice). Robin (1975) used a beat-interference technique to obtain  $v = 167.5 \pm 0.2 \text{ m } \mu\text{s}^{-1}$

**Table 1.** Location of RICE radio receivers. We have adopted the coordinate system convention used by the AMANDA collaboration. The transmitter is lowered into hole B4

Channel number	x m	y m	z m	Time delay ns
0	4.8	102.8	-166	1336
1	-56.3	34.2	-213	1416
2	-32.1	77.4	-176	1293
3	-61.4	85.3	-103	1230
4	-56.3	34.2	-152	1166
5	47.7	33.8	-166	1181
6	78.0	13.8	-170	944
7	64.1	-18.3	-171	939
8	43.9	7.3	-171	946
9	64.1	-18.3	-120	809
10 (B2)	43.9	7.3	-120	672
11 (B4)	67.5	-39.5	-168	952
12	66.3	74.7	-110	1051
13	-95.1	-38.3	-105	116
14	-46.7	-86.6	-105	1051
15	95.2	12.7	-347	1984
19	-95.1	-38.3	-135	1276

( $n = 1.79 \pm 0.01$ ), among the most precise measurements to date. Other experiments have used a variety of techniques (reflections off the bedrock, reflections off internal layers, etc.) to obtain values that vary from  $n = 1.71$  to  $1.79$ , although typical corrections are of order 2% and firn corrections are not applied uniformly (Bogorodsky and others, 1985, and references cited therein).

## METHODOLOGY AND EXPERIMENTAL APPARATUS

The RICE experiment at the South Pole presently consists of a multichannel array of radio receivers ('Rx'), scattered within a  $200 \text{ m} \times 200 \text{ m} \times 250 \text{ m}$  volume, at 100–350 m depths. Each receiver contains a 0.3 m long ( $l = 0.3 \text{ m}$ ) half-wave dipole antenna, offering good reception over the range 0.2–1 GHz. The peak response of the antenna is measured to be at  $\sim 450 \text{ MHz}$  in air ( $450 \text{ MHz}/n \sim 250 \text{ MHz}$  in ice), with a bandwidth  $\Delta f/f \sim 0.2$ . Antenna response can be quantified as a complex transfer function (or effective height)  $\mathbf{T}$  (m); given an incident electric field  $\vec{E}$ , the voltage  $V$  induced at the output of the antenna is given by  $V = \vec{E} \cdot \mathbf{T}$ . For a half-wave dipole antenna, the longest-wavelength resonance is expected at  $\lambda = 2l$ ; the magnitude of the effective height at resonance is expected to be of order  $l/\pi$  (Kraus, 1988; Balanis, 1997). Our measured antenna response is observed to be roughly reproducible from antenna to antenna and (roughly) consistent with expectation (Fig. 2).

The signal from each receiver antenna is immediately boosted by a 36 dB in-ice amplifier, then carried by  $\sim 300 \text{ m}$  coaxial cable to the surface observatory, where the signal is filtered (suppressing noise below 200 MHz due to both AMANDA phototubes and continuous-wave backgrounds from South Pole station at 149 MHz), re-amplified (either 52 or 60 dB gain), and split into two copies. One copy is fed into a (LeCroy Corporation) CAMAC electronics crate from which, after initial discrimination (using a LeCroy 3412

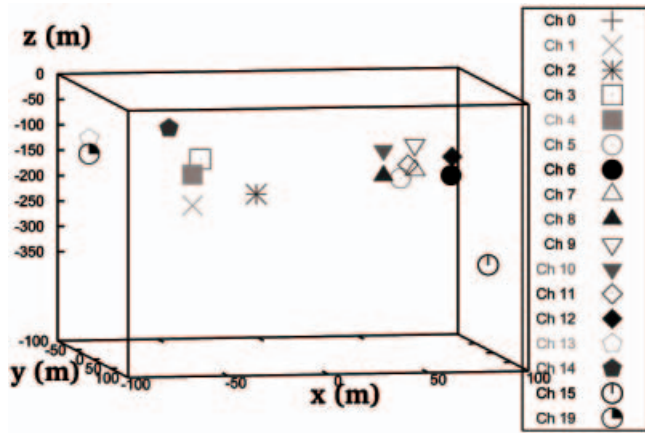


Fig. 3. Three-dimensional view of RICE receiver antenna array.

discriminator), the signal is routed into a Nuclear Instrumentation Methods (NIM) electronics crate where the trigger logic resides; a hit time is subsequently recorded by a LeCroy 3377 Time-to-Digital Converter (TDC) module for each receiver channel above threshold. The typical threshold is approximately a factor of five larger than the ambient thermal noise background  $\sigma_{kT}$ . The quoted timing resolution of the TDC module is 0.5 ns; this is verified in studies of the TDC 3377 using identical signals injected into two different channels of the TDC and comparing the recorded times in the two different channels. The other copy of the analog signal from an antenna is input to one channel of an HP54542 digital oscilloscope, where waveform information is recorded. Also deployed on the surface are three large transverse electromagnetic (TEM) horn antennas which are used to suppress surface-generated noise. Signals recorded in the TEM horns generate an inhibit signal which will blank out the data-acquisition system for the subsequent 3  $\mu$ s. For RF backgrounds generated on the surface, we expect hits to be first recorded in the TEM horns and then later (within 3  $\mu$ s) in the englacial dipole antennas.

## DETECTOR ARRAY GEOMETRY

The status of the current array deployment is summarized in Table 1 and Figure 3. Further details on detector geometry, deployment and calibration procedures are presented elsewhere (Kravchenko and others, 2003b).

For most of the measurements discussed in this paper, the transmitter was located at various depths in hole B4 (which also contains the channel 11 receiver), and broadcasting to the entire RICE receiver array. The Martin A. Pomerantz Observatory (MAPO, South Pole) building houses hardware for several experiments, including the RICE and AMANDA surface electronics, and is centered at ( $x \sim 40$  m,  $y \sim -30$  m) on the surface. The AMANDA array is located approximately 600 m (AMANDA-A) to 2400 m (AMANDA-B) below the RICE array in the ice; the South Pole Air Shower Experiment (SPASE) is located on the surface at ( $x \sim -400$  m,  $y \sim 0$  m). The coordinate system conforms to the convention used by the AMANDA experiment; grid north is defined by the Greenwich Meridian and coincides with the +y direction in the figure. The geometry of the receivers used for this measurement is also presented in Table 1.

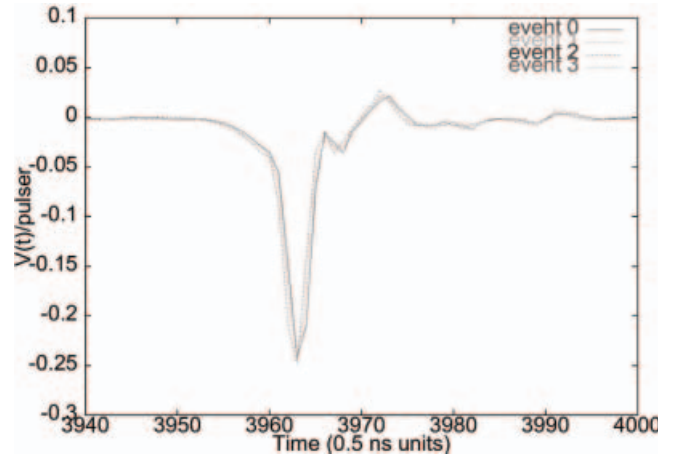


Fig. 4.  $V(t)$  trace for AVIR-1-C pulser input for transmitter signal used in this experiment, for four successive events. Reproducibility of signal  $t_0$  at  $t = 1981.5$  ns is evident. Horizontal binning is in units of 0.5 ns.

## EXPERIMENTAL PROCEDURE

In December 2002, two of the dry holes (B4 and B2, respectively) were uncovered by clearing away (i.e. shoveling) the 1.2–1.5 m deep snow cover which had accumulated in the intervening 4 years. The holes were found to be generally in the same condition as when they had originally been drilled. After hole B4 was uncovered, a  $\sim 300$  m length of coaxial cable was used to connect a transmitter (Tx) to a high-amplitude, fast rise-time pulse generator (AVTECH model AVIR-1-C) located within MAPO. One of the 20 oscilloscope input channels (four inputs on each of the five HP54542 digital oscilloscopes) was used to monitor the AVIR-1-C pulse-generator input and also to provide the overall start time ( $t_0$ ) for the recorded event. Figure 4 shows the monitored pulser signal ( $t_0$ ) for four successive events, indicating the reproducibility of the pulser output, as well as the fast rise time of the output signal.

After connecting one copy of the pulse generator to the dipole transmitter via the coaxial cable, the transmitter was lowered into hole B4. At either 5 m ( $-32$  m  $< z_{Tx}$ ) or 10 m ( $z_{Tx} < -132$  m) depth increments, a pulser signal (Fig. 4) was broadcast from the transmitter to the RICE receiver array, and signal arrival times in the receivers recorded (Fig. 5). (To check the reproducibility of our measurements, data were also recorded as the transmitter was later raised out of the hole.) Each pulser signal afforded two measurements of the index of refraction:

1. the index of refraction as a function of depth ( $n(z)$ ) was inferred by determining the transit time difference to a particular receiver between successive transmitter locations ( $n = c(t_i - t_j) / (|\vec{r}_{Tx,i} - \vec{r}_{Rx}| - |\vec{r}_{Tx,j} - \vec{r}_{Rx}|)$ ), with  $t_i$  the transit time corresponding to the transmitter at source location  $i$ ,  $t_j$  the transit time corresponding to the transmitter at source location  $j$ ,  $\vec{r}_{Tx,i}$  the vector defining the position of the transmitter at source location  $i$ ,  $\vec{r}_{Tx,j}$  the vector defining the position of the transmitter at source location  $j$ ,  $\vec{r}_{Rx}$  the vector defining the position of the (stationary) receiver, and  $c$  the velocity of light in a vacuum);
2. the ‘mean’ index of refraction ( $\langle n(\Delta z) \rangle$ ), averaged over the distance from the transmitter to any receiver, was

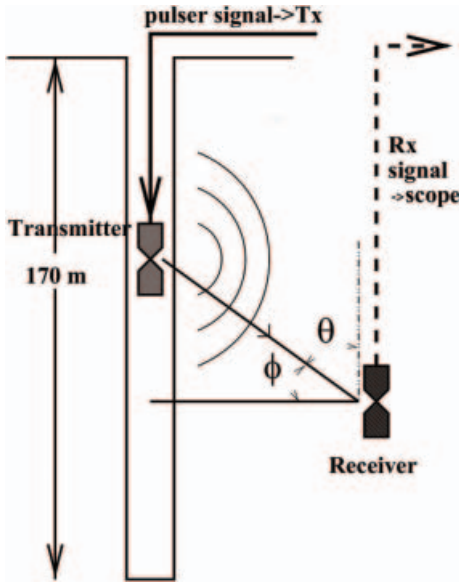


**Fig. 5.** Geometry of initial measurements. The transmitter (Tx) is connected, via coaxial cable, to a pulse generator or a continuous-wave generator in the MAPO. The transmitter broadcasts to one of the RICE dipole antennas (located in-ice). The angle  $\theta$  is measured relative to the  $z$  axis, and is the angle of incidence used in the Fresnel equations and for ray tracing. With this definition of angles, the expected dipole antenna beam pattern is then given by:  $E(\theta) \sim \sin \theta$ .

inferred knowing the time of the output pulser signal for each event ( $t_0$ ), the cable time delay between generator and transmitter ( $t_{Tx,gen}$ ), the cable time delay between receiver and data-acquisition system (DAQ) ( $t_{Rx,DAQ}$ ), and the time recorded for the  $i$ th receiver at the DAQ ( $t_{Rx,i}$ ) as:

$$\langle n \rangle = c(t_{Rx,i} - t_{Rx,DAQ} - t_0 - t_{Tx,gen}) / (|\vec{r}_{Tx,i} - \vec{r}_{Rx}|).$$

The former technique has the virtue of mapping out the index-of-refraction dependence on depth ( $n(z)$ ); the latter technique has the virtue of being less sensitive to transmitter location uncertainties as the transmitter is being lowered.

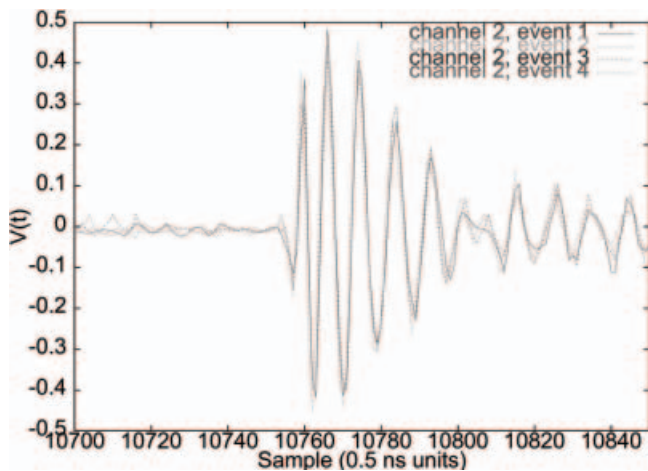


**Fig. 6.** Receiver waveforms recorded from channel 2 for four transmitter samples; for these data, the transmitter was located at  $-150$  m depth. Received signals are observed to be reproducible from event to event.

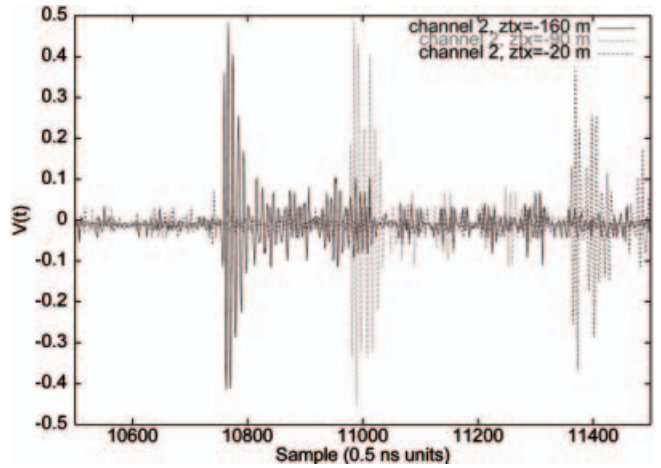


**Fig. 7.** Channel 2 waveforms recorded for transmitter at three different source depths. Horizontal axis is counts, in 0.5 ns bins. Vertical scale is recorded voltage. Although depths are equally spaced ( $-160$ ,  $-90$  and  $-20$  m), the hit times are not uniformly spaced since the receiver is not vertical with respect to the transmitter.

At each transmitter location, 20 successive transmitter pulses were broadcast. For each transmitter pulse, an  $8.192 \mu s$  waveform (sampled at  $2 GSa s^{-1}$ ) was captured in the digital oscilloscope, for each receiver. As noted before, the  $t_0$  of the transmitter signal was also recorded in one of the oscilloscope channels, to monitor possible timing shifts within the DAQ. Figure 6 illustrates the reproducibility of the receiver waveform for four typical samples corresponding to a given transmitter–receiver configuration.

**$n(z)$  DETERMINATION FROM RELATIVE RECEIVER HIT TIMES**

Figure 7 shows the migration (with time) of the direct-path hit times recorded in a typical channel (in this case, channel 2) of the RICE DAQ as the transmitting antenna is lowered into hole B4 (surface-reflected signals are discussed below). Several features are clear from this figure:

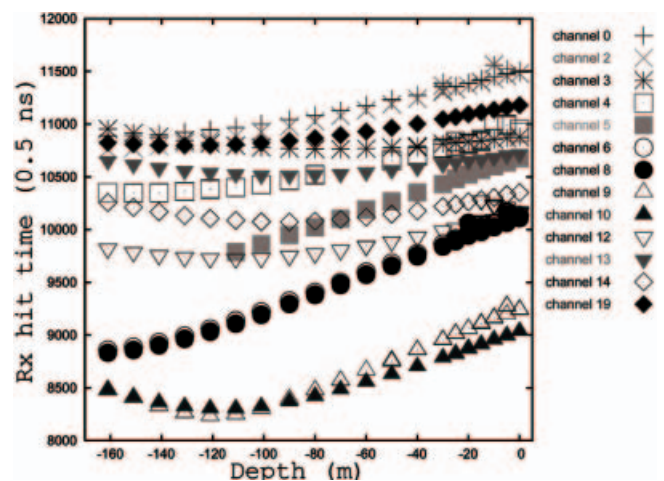


**Fig. 8.** Transmitter depth location vs recorded receiver hit times, for 13 different receivers. Channels are as indicated in the legend. The slope of each curve gives one determination of  $n(z)$ .

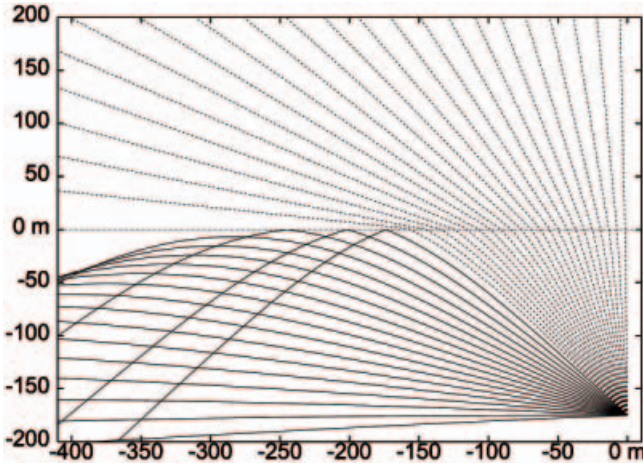


**Fig. 9.** Trajectories of rays (in the  $(r, z)$  plane) expected from a transmitter broadcasting from a depth of  $z = -170$  m.

(a) visually, the rise time of the signal can be measured to within  $\pm 1$  ns (two bins); (b) the signal shapes are not exactly reproducible at the various transmitter depths, suggesting ray-tracing complications due to the varying index of refraction or perhaps cross-talk effects; (c) although the angle of incidence relative to the receiver is changing substantially, the near-constancy of the peak amplitude suggests (given the sharp dependence of the Fresnel reflection coefficients with angle of incidence) that reflections off possible internal layers are not large.

The index of refraction is directly obtained from the electromagnetic wave propagation speed. At each transmitter depth, we record the hit time (discussed below); the variation in receiver hit times with transmitter depth is shown in Figure 8, for 13 receivers. The different shapes of these curves result primarily from differences in geometry between the various Tx–Rx pairs. (Note that each receiver can, in principle, be used to determine the index of refraction in the vicinity of the transmitter; in practice, the receivers which are closest to the axis of hole B4 (i.e. directly below or above) are geometrically best suited to make this measurement.) For each transmitter location, the electromagnetic wave propagation speed is directly obtained from the slopes in this figure, and can therefore be translated into an index-of-refraction profile,  $n(z)$ .

Before presenting numerical results, however, it is necessary to briefly consider the trajectories followed by rays in the ice, and possible complications due to our simplifying straight-line ray assumptions.

### Ray-tracing considerations

The trajectory of electromagnetic waves is determined by Fermat's least-time principle; a straightforward derivation can be used to obtain  $d\theta/dl = -(\partial n/\partial z)(\sin \theta/n)$ , with  $\theta$  the angle of incidence on the horizontal plane,  $dl$  a differential path length along the ray's trajectory, and  $\partial n/\partial z$  the gradient in the index-of-refraction with depth (the objective of this measurement). This expression leads to the (counter-intuitive) conclusion that even a ray directed horizontally along a contour of constant index of refraction will begin to bend into the region of higher index of refraction. Assuming a transmitter at  $-170$  m depth, below the nominal firn–ice transition, Figure 9 displays the expected ray tracing (based on our measured  $n(z)$  profile) up to a radial distance of

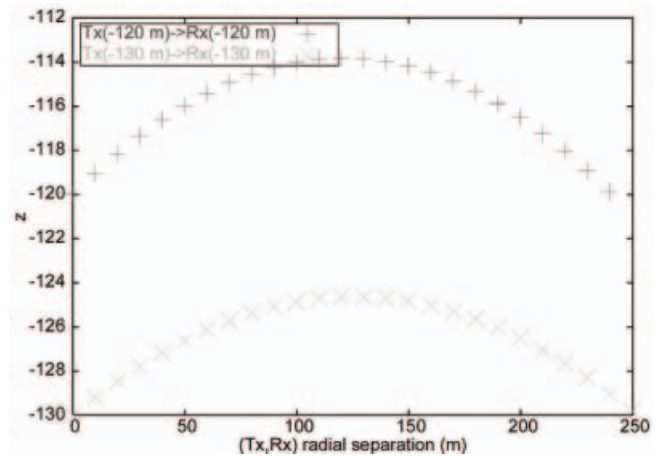


**Fig. 10.** Expected curvature of two rays connecting in-ice transmitter to in-ice receiver, with receiver and transmitter both at either  $-120$  or  $-130$  m in depth. Note the 10 : 1 aspect ratio of  $x$  vs  $y$  scales.

400 m from the source. Since, for our experiment, the transmitter–receiver distances are typically  $< 250$  m, such curvature effects are slight. Relevant to our experiment is the possibility that the effect of curvature on the difference of transit times between two source locations 5–10 m apart is larger than our typical measurement error ( $\sim 1$  ns). Figure 10 shows two sample trajectories, one connecting a hypothetical transmitter at  $z_{Tx} = -120$  m to a receiver at  $z_{Rx} = -120$  m, and another for  $z_{Tx} = -130$  m and  $z_{Rx} = -130$  m (note the aspect ratio between the  $x$  and  $y$  scales in the figure). Next (Fig. 11), along the trajectory of the rays shown, we can calculate the difference  $dt$  between the simple direct path vs the fully ray-traced path, as a function of the radial separation between transmitter and receiver for two cases. We observe that the correction ( $\sigma_{ray}$ ) for measurements made at successive transmitter locations (the difference between the two curves) is typically of order 0.5 ns or less; our conclusion is qualitatively consistent with previous estimates that the error in wave speed (as obtained from an  $x^2$  vs  $t^2$  plot) assuming straight-line ray tracing will be  $< 0.5\%$  (Bogorodsky and others, 1985). This correction is

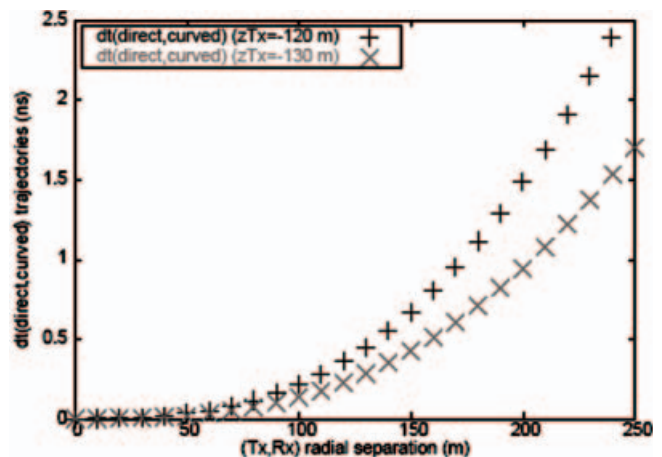


**Fig. 11.** Magnitude of time correction between transit time calculated for straight-line path vs transit time calculated with full ray tracing, along the trajectories shown in Figure 10.

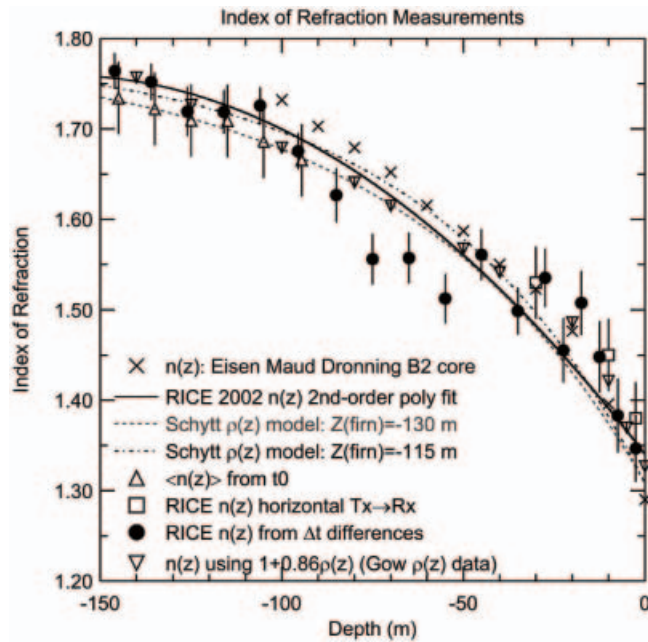


**Fig. 12.** Final fit to index-of-refraction data, combining information from all active receiver channels, and combining both up-going and down-going transmitter datasets. Statistical errors only are shown; inclusion of the systematic errors (estimated 4% at each point) would reduce the significance of the apparent ‘dip’ in the data points relative to the fitted curve around  $z \sim -80$  m to below  $2\sigma$  significance.

neglected for the subsequent analysis, but included in our determination of the total error  $\sigma_{\text{tot}}$ .

We point out that this correction is, unfortunately, non-linear: Suppose we take measurements in a receiver Rx, below the firn, at two different transmitter locations  $Tx_i$  and  $Tx_j$ . Measurement  $i$  is made with the transmitter in the firn, and measurement  $j$  is made with the transmitter below the firn; for each measurement there is a corresponding straight-line distance  $d_i$  or  $d_j$  to the receiver. No ray-tracing corrections are applicable for  $Tx_j \rightarrow Rx$ ; however, for  $Tx_i \rightarrow Rx$ , the actual curved trajectory  $d_i$  is longer than the straight-line trajectory. Since we have used  $c/n = (d_i - d_j)/(t_i - t_j)$ , with  $t_i - t_j$  the measured hit-time difference, inserting the true (larger) curved path length  $d_i$  has the effect of reducing the calculated value of  $n$ . This is expected since the curved trajectory, by Fermat’s principle, preferentially samples shallower, lower index-of-refraction ice. By neglecting this effect, we therefore slightly overestimate both the index of refraction and the appropriate measurement depth. To some extent, these two effects tend to offset each other.

## MEASUREMENT UNCERTAINTIES

Known uncertainties arise from the following sources:

1. The temperature dependence of the index of refraction of cold ice has been measured, although it has been shown to be a small ( $\sim 1\%$ ) effect, from  $0^\circ\text{C}$  to  $-60^\circ\text{C}$  (Gough, 1972; Johari and Charette, 1975; Mätzler and Wegmüller, 1987). Over the first 150 m of the ice, the temperature variation is expected to be  $< 5^\circ\text{C}$ . The corresponding effect on measurements taken from any two successive transmitter locations is therefore expected to be insignificant.

2. There is some uncertainty associated with discerning the actual hit time. To minimize this, the 20 events recorded on each receiver from each transmitter height were added, in order to enhance signal-to-noise, and the signal arrival times were also extracted by visual inspection of the summed waveforms. Alternately, the receiver arrival times can be determined from various software algorithms. The simplest algorithm simply picks out the first  $6\sigma_{\text{kT}}$  excursion in a waveform, where  $\sigma_{\text{kT}}$  is the rms noise in the waveform outside the signal region, dominated by thermal noise. More sophisticated algorithms calculated the  $\chi^2$  between the receiver signal and the expected signal shape (knowing the transfer function described previously), and selected the time in the waveform which gave the lowest  $\chi^2$ , or selected the first time in the waveform for which at least four of any eight sequential samples corresponded to  $> 4\sigma_{\text{kT}}$ . ‘Good’ data were required to satisfy the requirement that the variation  $\sigma_{\text{hit}}$  between the four algorithms was  $< 1$  ns.
3. Since the transmitter depths were determined using the length markings directly on the cable, which was marked in both 1 ft and 1 m intervals, additional measurement uncertainties arise from transmitter depth uncertainties ( $< 0.5$  m) at each transmitter location. Survey errors in the locations of each receiver are estimated at  $\sim 1$  m per receiver.

## RESULTS

We have attempted to obtain an aggregate estimate of  $n(z)$  by:

1. averaging the raising-transmitter plus lowering-transmitter datasets;
2. averaging all highest-quality data from all possible channels, where the contribution to the final average from each channel was weighted by geometry and favoring nearly vertical receiver channels (the error was assessed here as  $1/\sigma_{\text{geometry}}^2 = (t_i - t_{i+1})^2$ , where  $t_i$  and  $t_{i+1}$  are the calculated transit times for the measurements  $i$  and  $i + 1$ . Cases where the times are approximately the same for two successive measurements, i.e. the receiver and transmitter are at approximately the same depth, are therefore substantially deweighted) and reproducibility of the extracted hit time (favoring cases where the software algorithm found the same hit time for all of the 20 events taken at one transmitter location). An rms error,  $\sigma_{20}$ , was determined for the 20 measurements, and a requirement that this rms value be  $< 1$  ns (two waveform samples) was imposed, after requiring consistency among the four hit-time algorithms;
3. reducing the effect of uncertainties in the transmitter locations by re-obtaining averages taking the data obtained for 10–20 m distance differences (rather than 5–10 m) between successive Tx broadcasts. That is, we calculate  $n(z)$  using  $t_{Tx,i}$  relative to  $t_{Tx,i+2}$  rather than relative to  $t_{Tx,i+1}$  and therefore reduce the ratio of the time error arising from uncertainties in the transmitter location relative to the difference in propagation time between successive measurements. We would expect this procedure to correct for cases where the transmitter may have been slightly higher or lower than recorded for the intervening measurement.

**Table 2.** Data used to extract asymptotic value of  $n(z)$ 

Tx delay ns	Rx delay ns	Rx $t_{\text{hit}}$ ns	$\Delta t$ ns	$\Delta d$ m	$v$ $\text{m s}^{-1}$	$n$
1432	1984	4785	$1369 \pm 8$	$233 \pm 2$	$1.70 \times 10^8$	$1.764 \pm 0.021$

The difference between these coarse-grained measurements and the default finer-grained measurements contributed another error  $\sigma_{\Delta z}$ . Because the index-of-refraction profile is non-linear, the coarse-grained measurements tend to underestimate the index of refraction in the vicinity of the transmitter, so these measurements are not used directly, but are only used to determine an associated error. We then calculate a total error  $\sigma_{\text{tot}}$ , which is the inverse quadrature sum of all the errors cited above, at each transmitter location ( $1/\sigma_{\text{tot}}^2 = 1/\sigma_{20}^2 + 1/\sigma_{\text{hit}}^2 + 1/\sigma_{\text{ray}}^2 + 1/\sigma_{\text{geometry}}^2 + 1/\sigma_{\Delta z}^2$ ). Figure 12 shows the result of this procedure, and also includes data obtained by broadcasting horizontally between a transmitter being lowered into hole B4 and a receiver being lowered into hole B2. Also included are measurements derived from the ‘mean’  $n(z)$  values obtained using absolute  $t_0$  measurements, which average over the  $n(z)$  profile between transmitter and each receiver, as well as comparisons with the predictions of the Schytt model for density and  $n(z) = 1 + 0.86\rho(z)$ , assuming alternately that the ice–firn transition occurs at  $z = -115$  m and at  $z = -130$  m.

The RICE data points are fit to a second-order polynomial ( $n(z) = 1.324 - 5.2854z - 21.865z^2 - 39.058z^3$ ;  $z$  is in km for this parameterization), with the assumption that the value of index of refraction at large depths approaches a constant. We obtained an estimate of that asymptotic value by broadcasting from the deepest buried RICE transmitter ( $x = -85$  m,  $y = 8$  m,  $z = -200$  m) down to the deepest buried RICE receiver (channel 15); both of these antennas are presumably well below the firn–ice transition. Those data are presented in Table 2, and are included in our fit.

This asymptotic value is in fair agreement with the accepted value of 1.78, as obtained by several measurements (Evans, 1965; Gudmandsen, 1971; Hempel and others, 2000). The confidence level of the fit to all the RICE data points in Figure 12, using just the previously tabulated errors ( $\sigma_{\text{tot}}$ ), is rather small (3.1%). In order to achieve a confidence level of 50% requires an error, per data point, of 4%. We take this to be a conservative estimate of the overall (systematic plus statistical) error, point-to-point, on the measurement. Our data favor a non-linear variation of index of refraction with depth, albeit only slightly: fitting  $n(z)$  to a linear form ( $n(z) = c_0 + c_1 z$ ) results in an increase in  $\chi^2/\text{degree-of-freedom}$  of only 0.15.

## CROSS-CHECKS

### Possible cable cross-talk with pre-existing cables

Although the cable connected to the receiver (at  $-170$  m depth) also located in hole B4 (channel 11) is shielded coax, and is therefore not expected to have substantial pick-up from the transmitter in the same hole, we explicitly checked

this in two ways. First, we directly calculated the vertical signal propagation speed based on the recorded arrival time in the channel 11 B4 receiver at  $z = -170$  m, when the transmitter was located near the top of the hole. This was determined as  $v \sim c/1.59$  ( $\sim 190 \text{ m } \mu\text{s}^{-1}$ ); since the signal propagation speed through the cable is known to be  $0.88c$ , direct propagation through the cable down to channel 11 rather than the ice would lead to  $v \sim c/1.14$ . (Note that the diameter of hole B4 is substantially smaller than the wavelengths being broadcast from transmitter to receiver.) Additionally, we compared signal propagation speeds in the case when the signal was broadcast from B4 to a receiver dipole antenna placed in the 1998 station Rodriguez well hole (approximately 255 mm in diameter, but without any cables or equipment, located at  $(x, y) = (+16 \text{ m}, +36 \text{ m})$ ), to the case where we broadcast from a transmitter in B4 to an additional receiver being lowered in tandem in hole B2 (approximately 50 m radially displaced, and also having a cable and a pre-existing RICE receiver). For this set of measurements, broadcasts were made directly horizontally, and direct time measurements taken. For depths down to 30 m ( $z = -5$  m,  $-15$  m and  $-30$  m), these were also found to be consistent with our other previously mentioned  $n(z)$  results. Finally, we compared signal propagation speeds from a transmitter to RICE receiver channel 15, in the case when the transmitter was located in hole B4 vs the case when the transmitter was located in the hole above the Rodriguez well. These were also found to be consistent with each other.

### Check that $v = c$ in air

An elevated (above-surface) transmitter was used to broadcast in-air to an elevated receiver, over baselines varying from 24 to 48 m. On successive trials, propagation speeds were measured to be:  $2.875 \times 10^8$ ,  $3.125 \times 10^8$ ,  $3.0875 \times 10^8$  and  $3.125 \times 10^8 \text{ m s}^{-1}$ . These measurements are consistent with  $v = (1.02 \pm 0.02)c$ , and to some extent also set the scale of the inherent measurement errors.

## COMMENT ON REFLECTIONS

The possibility of multiple paths connecting transmitter to receiver suggests the possibility that we might observe after-pulses (or ‘double pulses’). The simplest reflected path is expected to be a path which corresponds to an upward-directed ray from a transmitter, bouncing off the top surface ice–air discontinuity, and back down to a buried receiver. We have searched for reflections by looking for after-pulses in the captured waveforms after the initial hit times (as shown in Fig. 13). In the ‘surface reflection’ model, we expect the time delay between the first and second pulses to increase with transmitter depth. We observe after-pulses in all channels. These measurements also offer a check of our ray-tracing algorithm. Figure 14 compares the expected time



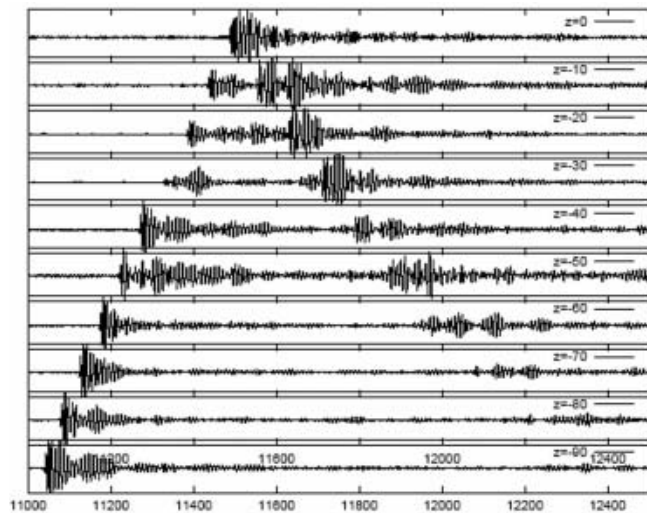


**Fig. 13.** Successive voltage signals (corresponding to increasing depths) observed for transmitter broadcasting to channel 0 of the RICE data-acquisition system. Note the systematic increase in time delay between primary and after-pulse as the transmitter depth increases. Horizontal scale is in units of 0.5 ns.

delay between the initial pulse and the after-pulse with the observed time delay, for four different channels. Within our ability to visually discern the hit time of the after-pulse, we find reasonable agreement between our ray-tracing model and the data. In principle, a timing analysis and an amplitude analysis (using the Fresnel equations) could be used to independently determine the index-of-refraction profile up to the surface, and the index-of-refraction discontinuity at the surface, respectively. Such efforts are currently in progress.

### COMMENT ON INTERNAL LAYER REFLECTIONS

Layers can arise as a result of episodic events (e.g. dust or acid layers due to volcanic eruptions) or annual processes, including thin surface crusts which form in the summer, constituting a discontinuity in density. Layers of the latter type should become less important with depth as the ice approaches its asymptotic density. Anisotropies in the crystal structure of the ice may also constitute a discontinuity. Nearer to the coast, brine infiltration can also result in stratified layering. However, this is expected to be negligible at the South Pole. Precise study of layers requires extremely sensitive receivers and, in the case of annual layering, the ability to distinguish density differences of order 1–10 cm apart (<1 ns) in the ice. Interferometry or pulse modulation techniques can also be used to probe layering, provided the interferometer is sensitive to 1 ns time-scales. Such exacting requirements have hampered a complete understanding of internal layering thus far using GPR data. In addition to discrete layers, quasi-continuous  $\lambda^{-4}$  Rayleigh scattering off air bubbles in unenclathrated ice has been considered quantitatively (Smith and Evans, 1972), resulting in a ‘worst-case’ estimate of an attenuation loss of  $0.7\lambda^{-4}$  dB per 100 m.

Reflections off internal layers can modify the ray tracing required in our extraction of  $n(z)$ . Although we can detect the surface reflections shown in Figure 13, we have insufficient sensitivity to directly observe reflections off

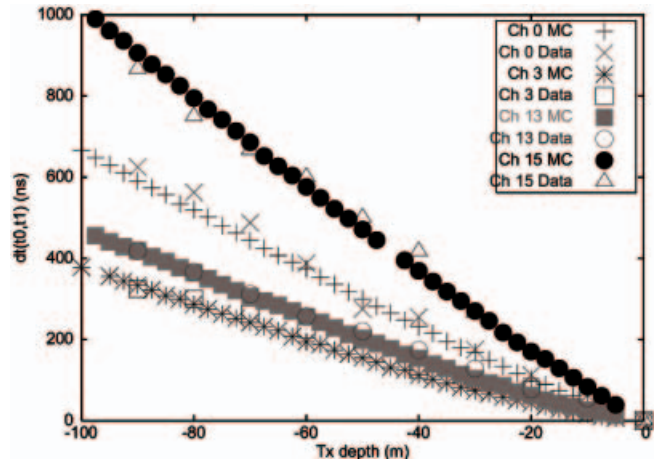


**Fig. 14.** Modeled vs measured values of the expected time delay between direct-path pulse and after-pulses due to surface reflections observed in our transmitter data.

internal layers. Such layers have previously been observed (using GPR) as low-power (typically,  $-60$  to  $-80$  dB) returns from within and below the firn. Bogorodsky and others (1985) suggest an ‘equivalent-layer’ model consisting of 1 mm thick layers spaced  $\sim 1$ – $10$  m apart, with a dielectric contrast  $\Delta\epsilon/\epsilon = 0.002$ , or  $\Delta n/n = 0.001$  between successive layers. We have attempted to test such a model by plotting the amplitude of the received signals (in units of  $\sigma_{kT}$ ), as a function of the angle of incidence of rays traced from the transmitter, as it is being lowered, to a receiver (for simplicity, we have assumed straight-line trajectories for this exercise). Although layers can ‘trap’ signal, possibly resulting in an amplified received signal, we expect that such trapped signals may (depending on the incident angles) arrive at the receivers asynchronously with the primary hit, and neglect such effects in our analysis. We also neglect any second-order reflections, i.e. transmission through layer 1 followed by reflection off layer 2 (with possible subsequent interference effects). Figure 15 displays the Fresnel-derived transmitted amplitudes for 1 m layering, assuming a density contrast of 0.001 for successive layers, as a function of the incidence angle  $\theta$ . Curves are presented for various values of vertical displacement  $dz$  between Tx and Rx. In this scheme, traversal of multiple layers results in a multiplicative, rather than a linear, loss of signal amplitude (in practice, there would be ‘thin-film’-type interference between the signals arriving from (multiple) reflections within the ice; we neglect such effects for the purpose of this simplified analysis). The model includes the dipole antenna beam pattern ( $E(\theta) \sim \sin \theta$ , or, equivalently,  $E(\phi) \sim \cos \phi$ ), and also takes into account the  $1/r$  loss of amplitude with distance from receiver, to allow a direct comparison with data. Figure 16 shows the ensemble of all recorded data (all recorded signals for all receiver data, in units of  $kT$  thermal noise): for values less than the threshold predefined for ‘good’ hits in this analysis ( $\text{Signal} > 22.5\sigma_{kT}$ ), the times are considered unreliable and are not used in the index-of-refraction calculation. Such amplitudes are assigned a value of zero in Figure 16a. If there are significant losses due to the reduced Fresnel transmission amplitudes at ‘glancing angles’, we would expect to see a reduction in the average signal strengths recorded as  $\cos \theta \rightarrow 0$ , as well as an increase in the number of recorded signals entered as zeroes. Our

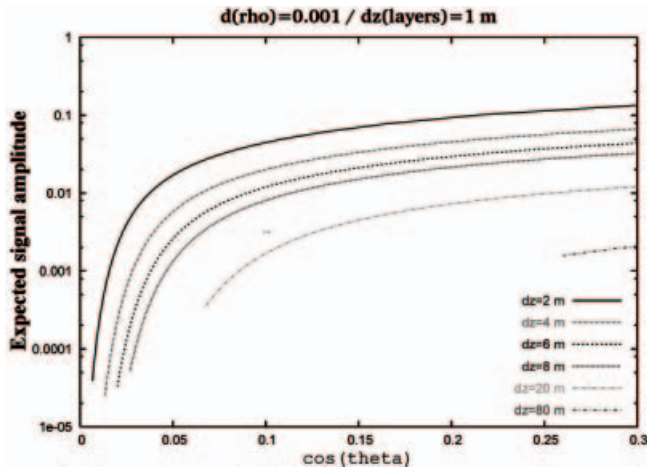


**Fig. 15.** Predicted transmission coefficient, as a function of incident angle, and vertical displacement of transmitter relative to a receiver.

data show no dramatic decrease of signal as  $\cos\theta \rightarrow 0$  ( $\theta \rightarrow \pi/2$ ), as would be expected in the multiple scattering-layer model depicted in Figure 15. Figure 16b shows a zoom of the region around  $\cos\theta \sim 0$  using receivers which sample depths both above and below the transmitter. Again, our data do not indicate significant signal loss due to internal reflections. This is perhaps not entirely unexpected: since we are in a regime where  $\lambda \gg t_{\text{layer}}$ , with  $t_{\text{layer}}$  the physical thickness of each layer, one might anticipate mitigation of internal scattering effects.

### COMMENT ON BIREFRINGENCE

We note that, in principle, the ice can be birefringent, this birefringence being either ‘linear’ (linear propagation velocities different along two perpendicular axes in the ice; presumably the symmetry axis is defined by gravity in the upper few hundred meters at the South Pole) or ‘circular’ (in the case where there is some rotational asymmetry in the crystal structure, for which the propagation velocities of the left- and right-circular polarizations will differ). Since both transmitter and receiver have the same polarization axis (antennas are oriented vertically within the ice holes), we are insensitive to linear birefringent effects. Since circular birefringence results in a separation between the left- and right-circular polarizations, and a rotation of the plane of polarization as the signal moves through the ice from the transmitter, we would expect that the received signal strength would depend on the orientation of the polarization axis at the location of each receiver. The fact that the signal received from a transmitter by each receiver does not obviously show such effects provides circumstantial evidence that circular birefringent effects are not large (Kravchenko and others, 2003b).

### CONCLUSION

We have used the RICE array at the South Pole to measure the index of refraction through the firm. We obtain an index-of-refraction profile ( $n(z)$ ) which qualitatively agrees with that extrapolated from direct laboratory studies of the electrical properties of ice cores. We are also consistent with the expected correlation of  $n(z)$  with ice density  $\rho$ . We note that, since the firm–ice transition corresponds to

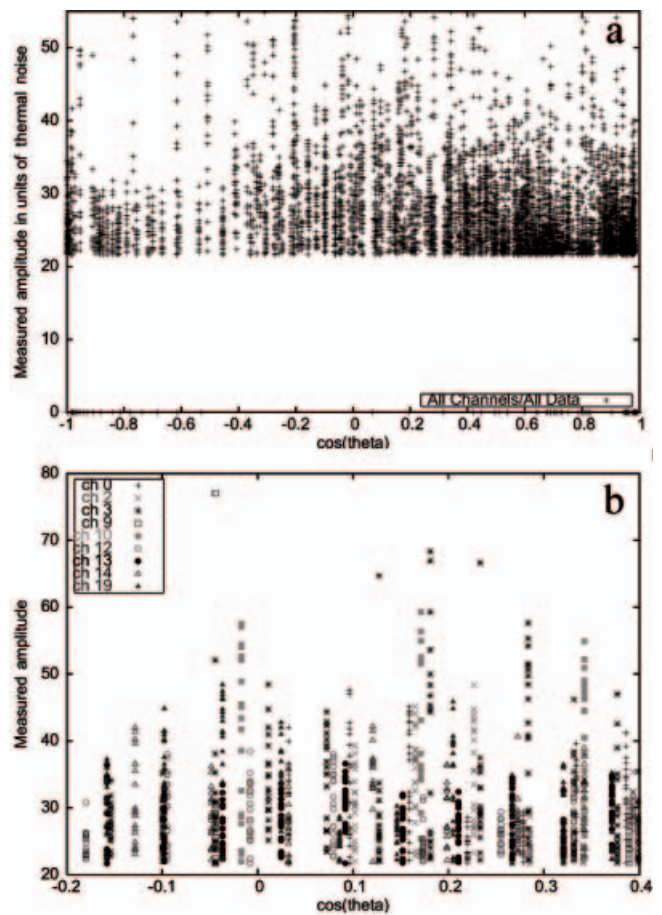


**Fig. 16.** (a) Raw peak receiver amplitude data recorded for all  $T_x \rightarrow R_x$  combinations, as a function of angle  $\theta$ . If the recorded receiver amplitude is  $< 22.5\sigma_{kT}$ , a value of zero is entered in this plot. (b) Zoom of data recorded in the region  $\cos\theta \approx 0$ , where Fresnel losses off possible internal layers should be maximal. Note that positive (negative) values of  $\cos\theta$  correspond to cases for which the transmitter is higher (lower) than the receiver; for the Monte Carlo simulation shown in Figure 15, we have only simulated geometries for which the transmitter is higher than the receiver.

$\rho \sim 830 \text{ kg m}^{-3}$ , we can use the linear dependence of the refractive index on density to infer a firm–ice transition depth of  $z \sim -100 \text{ m}$  from our data, although values down to  $z \sim -130 \text{ m}$  are allowed, given our errors. Our results have implications for experiments which rely on the detection of radio waves propagating through the firm. This includes GPR probes of the ice sheet, which translate a measured time delay into a depth, and also includes experiments based on the detection of radio waves from neutrino-induced electromagnetic showers in the ice.

The measurement technique, however, has limitations due to the finite bandwidth of the antennas and data-acquisition system we have used, which smears the measured signal onset in the time domain. An improved in situ measurement would utilize higher-bandwidth electronics, thus permitting higher-resolution software techniques (matched filters) to improve the timing granularity well beyond the intrinsic sampling time of the measurement hardware.

In the austral summer 2003/04, efforts were focused on measurements of the imaginary (absorptive) component of the dielectric constant. Results on those measurements are currently in preparation.

## ACKNOWLEDGEMENTS

We are indebted to our other RICE collaborators for suggestions, ideas and instructive comments, as well as the AMANDA and SPASE collaborations for their logistical support since 1995. Raytheon Polar Services provided essential logistical support for this effort. K. Mueller assisted with a trial version of this experiment, conducted in January 2002. J. Drees assisted in the clearing of the holes used for this measurement. We are indebted to M. Peters of the University of Texas Institute of Geophysics, who provided indispensable antenna engineering expertise. We thank the US National Science Foundation's Office of Polar Programs for support under grant NSF OPP-0085119, the Research Corporation, the University of Kansas Undergraduate Research Award Program, the NSF's Research Experience for Undergraduates (REU) program, and the University of Kansas Center for Research Inc. (CRINC). The insightful comments of two anonymous referees were indispensable in crafting the final version of this text.

## REFERENCES

- Ahrens, J. and 116 others. 2003a. Search for neutrino-induced cascades with the AMANDA detector. *Phys. Rev., Ser. The AMANDA collaboration*, **D67**(2003), 012003.
- Ahrens, J. and 107 others. 2003b. Search for point sources of high energy neutrinos with AMANDA. *Astrophys. J., Ser. The AMANDA collaboration*, **583**(2), 1040–1057.
- Ahrens, J. and 113 others. 2003c. Limits on diffuse fluxes of high energy extraterrestrial neutrinos with the AMANDA-B10 detector. *Phys. Rev. Lett., Ser. The AMANDA collaboration*, **92**(2004), 071102.
- Balanis, C. 1997. *Antenna theory, analysis and design. Second edition*. New York, John Wiley and Sons.
- Bogorodsky, V.V., C.R. Bentley and P.E. Gudmandsen. 1985. *Radioglaciology*. Dordrecht, etc., D. Reidel Publishing Co.
- Clarke, T.S. and C.R. Bentley. 1994. High-resolution radar on Ice Stream B2, Antarctica: measurements of electromagnetic wave speed in firn and strain history from buried crevasses. *Ann. Glaciol.*, **20**, 153–159.
- Costas, N. 1963. On the process of normal snow densification in an ice cap. In Kingery, W.D., ed. *Ice and snow: properties, processes and applications*. Cambridge, MA, MIT Press, 237–247.
- Dodd, R.T. 1989. Unique find from Antarctica. *Nature*, **338**(6213), 296–297.
- Eisen, O., F. Wilhelms, U. Nixdorf and H. Miller. 2003. Revealing the nature of radar reflections in ice: DEP-based FDTD forward modeling. *Geophys. Res. Lett.*, **30**(5), 1218–1221. (10.1029/2002GL016403.)
- Evans, S. 1965. Dielectric properties of ice and snow – a review. *J. Glaciol.*, **5**(42), 773–792.
- Fujita, S., T. Matsuoka, T. Ishida, K. Matsuoka and S. Mae. 2000. A summary of the complex dielectric permittivity of ice in the megahertz range and its applications for radar sounding of polar ice sheets. In Hondoh, T., ed. *Physics of ice core records*. Sapporo, Hokkaido University Press, 185–212.
- Gough, S.R. 1972. A low temperature dielectric cell and the permittivity of hexagonal ice to 2 K. *Can. J. Chem.*, **50**(18), 3046–3051.
- Gudmandsen, P.E. 1971. Electromagnetic probing of ice. In Wait, J.R., ed. *Electromagnetic probing in geophysics*. Boulder, CO, Golem Press, 321–348.
- Hecht, E. 2001. *Optics. Fourth edition*. New York, Addison-Wesley.
- Hempel, L., F. Thyssen, N. Gundestrup, H.B. Clausen and H. Miller. 2000. A comparison of radio-echo sounding data and electrical conductivity of the GRIP ice core. *J. Glaciol.*, **46**(154), 369–374.
- Johari, G.P. and P. Charette. 1975. The permittivity and attenuation in polycrystalline and single-crystal ice Ih at 35 and 60 MHz. *J. Glaciol.*, **14**(71), 293–303.
- Karle, A. 2002. IceCube – the next generation neutrino telescope at the South Pole. In *Proceedings of the XXth international conference on neutrino physics and astrophysics. Munich, Germany, 25–30 May 2002*. F. von Feilitzsch and N. Schmitz, eds. *Nucl. Phys. B (Proceedings supplements)* **118**(2003), 388–395.
- Kraus, J. D. 1988. *Antennas*. New York, McGraw-Hill.
- Kravchenko, I. and 19 others. 2003a. Limits on the ultra-high energy electron neutrino flux from the RICE experiments. *Astroparticle Physics*, **20**, 195–213.
- Kravchenko, I. and 14 others. 2003b. Performance and simulation of the RICE detector. [The RICE Collaboration.] *Astroparticle Physics*, **19**, 15–36.
- Mätzler, C. and U. Wegmüller. 1987. Dielectric properties of freshwater ice at microwave frequencies. *J. Appl. Phys.*, **20**(12), 1623–1630.
- Moore, J.C. and J.G. Paren. 1987. A new technique for dielectric logging of Antarctic ice cores. *J. Phys. (Paris)*, **48**, Colloq. C1, 155–160. (Supplément au 3.)
- Narita, H., N. Maeno and M. Nakawo. 1978. Structural characteristics of firn and ice cores drilled at Mizuho station, East Antarctica. *Mem. Nat. Inst. Polar Res. Spec. Issue* 10, 48–61.
- Niessen, P. 2003. Recent results from the Antarctic muon and neutrino detector array experiment. In *Proceedings of the 38th Rencontres de Moriond. Les Arcs, France, 15–22 March 2003*, 243–248.
- Oerter, H. and 6 others. 2000. Accumulation rates in Dronning Maud Land, Antarctica, as revealed by dielectric-profiling measurements of shallow firn cores. *Ann. Glaciol.*, **30**, 27–34.
- Paterson, W.S.B. 1994. *The physics of glaciers. Third edition*. Oxford, etc., Elsevier.
- Robin, G.deQ. 1975. Velocity of radio waves in ice by means of a bore-hole interferometric technique. *J. Glaciol.*, **15**(73), 151–159.
- Schytt, V. 1958. Glaciology II(C). The inner structure of the ice shelf at Maudheim as shown by core drilling. *Norwegian–British–Swedish Antarctic Expedition, 1949–52. Sci. Results*, **IV**, 113–151.
- Smith, B.M.E. and S. Evans. 1972. Radio echo sounding: absorption and scattering by water inclusion and ice lenses. *J. Glaciol.*, **11**(61), 133–146.
- Wilhelms, F. 2000. Messung dielektrischer Eigenschaften polarer Eiskerne. *Ber. Polarforsch./Rep. Pol. Res.*, **367**, 1–171.
- Wilhelms, F., J. Kipfstuhl, H. Miller, K. Heinloth and J. Firestone. 1998. Precise dielectric profiling of ice cores: a new device with improved guarding and its theory. *J. Glaciol.*, **44**(146), 171–174.